Spectro-astrometry with MEGARA/GTC: a pilot study to search for protoplanets

Brčić, Paula

Master's thesis / Diplomski rad

2022

Degree Grantor / Ustanova koja je dodijelila akademski / stručni stupanj: **University of Split, Faculty of Science / Sveučilište u Splitu, Prirodoslovno-matematički fakultet**

Permanent link / Trajna poveznica: https://urn.nsk.hr/urn:nbn:hr:166:624147

Rights / Prava: In copyright/Zaštićeno autorskim pravom.

Download date / Datum preuzimanja: **2025-02-19**

Repository / Repozitorij:

Repository of Faculty of Science

University of Split

Faculty of Science

Spectro-astrometry with MEGARA/GTC: a pilot study to search for protoplanets

Master thesis

Paula Brčić

Split, September 2022

I would like to thank my supervisor Dr. Koraljka Mužić for her wonderful classes and seminars, in which I learned more in one hour than in a semester of other subjects. Thank you for connecting me with my mentors, and for your help with this thesis.

I am extremely grateful to my mentors Dr. Nuria Huélamo Bautista and Dr. Ignacio Mendigutía for their knowledge, encouragement, support, and patience during this work. Thank you for all your comments and corrections, through which I learned more than I ever expected in just a few months.

The warmest thank you to everyone at CAB (CSIC-INTA) for making me feel at home, and for helping me practice my Spanish.

Lastly, a big thank you to my family and friends for always being there for me, regardless of any distance.

Spektro-astrometrija s instrumentom MEGARA/GTC: pilot-studija u potrazi za protoplanetima

Paula Brčić

Sveučilišni diplomski studij Fizika; Astrofizika i fizika elementarnih čestica

Sažetak:

Otkrivanje formirajućih planeta u protoplanetarnim diskovima vrlo je izazovno i veliki je cilj moderne astrofizike. Emisija H_{α}, koja je vjerojatno povezana s LkCa 15 b, čini ovaj potencijalno akretirajući planet prvim ikada objavljenim, iako nije jednoznačno potvrđen. Spektro-astrometrija (SA) je promatračka tehnika kojom je moguće mjeriti relativne položaje ovisne o valnoj duljini s ekstremnom preciznošću, a nedavno se pokazala obećavajućom za otkrivanje akretirajućih protoplaneta.

Cilj ovog rada je istražiti je li SA s MEGARA instrumentom na 10.4 m Gran Telescopio de Canarias (GTC) prikladan za otkrivanje akretirajućih protoplaneta. Tehnika je testirana ovim instrumentom koristeći promatranja dviju zvijezda, uključujući LkCa 15.

Pokazujemo valjanost tehnike s MEGARA-om na temelju dobro poznate binarne zvijezde GU CMa, dobivajući SA signale u skladu s prethodnim radovima. Iako opažanja LkCa 15 postižu potrebnu SA preciznost, instrumentalni artefakti najvjerojatnije utječu na promatrane signale i sprječavaju nas u donošenju čvrstih zaključaka o mogućem protoplanetu. Provedeni su testovi kako bi se istražilo njihovo podrijetlo, ali potreban je daljnji rad kako bismo u potpunosti razumjeli naša opažanja prije nego što se MEGARA može koristiti u SA načinu rada za rutinsko traženje akretirajućih protoplaneta.

Spectro-astrometry with MEGARA/GTC:
a pilot study to search for protoplanets

Paula Brčić

University graduate programme Physics; Astrophysics and Elementary Particle Physics

Abstract:

The detection of forming planets in protoplanetay disks is very challenging and a major goal in modern astrophysics. The H_α emission presumably associated to LkCa 15 b makes this potential accreting planet the first ever reported, although it is not unambiguously confirmed. Spectro-astrometry (SA) is an observational technique capable of measuring wavelength-dependent relative positions with extreme accuracy, and has recently shown promise for detecting accreting protoplanets.

The aim of this work is to investigate if SA carried out with the MEGARA instrument at the 10.4 m Gran Telescopio de Canarias (GTC) is suitable for detecting accreting protoplanets. The technique is tested with this instrument using observations of two stars, including LkCa 15.

We demonstrate the validity of the technique with MEGARA based on the well known binary star GU CMa, recovering SA signals consistent with previous works. Although the observations of LkCa 15 achieve the required SA precision, instrumental artifacts are most probably affecting the observed signals and prevent us from reaching firm conclusions about the possible protoplanet. Tests were done to investigate their origin, but further work is required to fully understand our observations before MEGARA can be used in SA mode to routinely search for accreting protoplanets.

Contents

1   Introduction

1.1   Protoplanet formation

After the birth of a star through gravitational collapse, circumstellar disks of gas and dust form due to the conservation of angular momentum. Disk lifetime is usually a few Myr, which is a stringent upper limit to the timescale of planet formation (Haisch et al. 2001).

In the first stage the disk is flared outwards and material is being accreted onto the star. Far ultraviolet (FUV) photons cause photoevaporation in the outer parts of the disk (see Figure 1). The micrometer-sized dust grains start coagulating together, sedimenting towards the mid-plane of the disk and drifting towards the star. As extreme ultraviolet (EUV) radiation begins to dominate, it clears the inner disk of material which can no longer be resupplied from the outer parts, eventually forming an inner hole. Smaller particles continue photoevaporating until a debris disk of large grains, planetesimals and possibly planets remains (Williams & Cieza 2011).
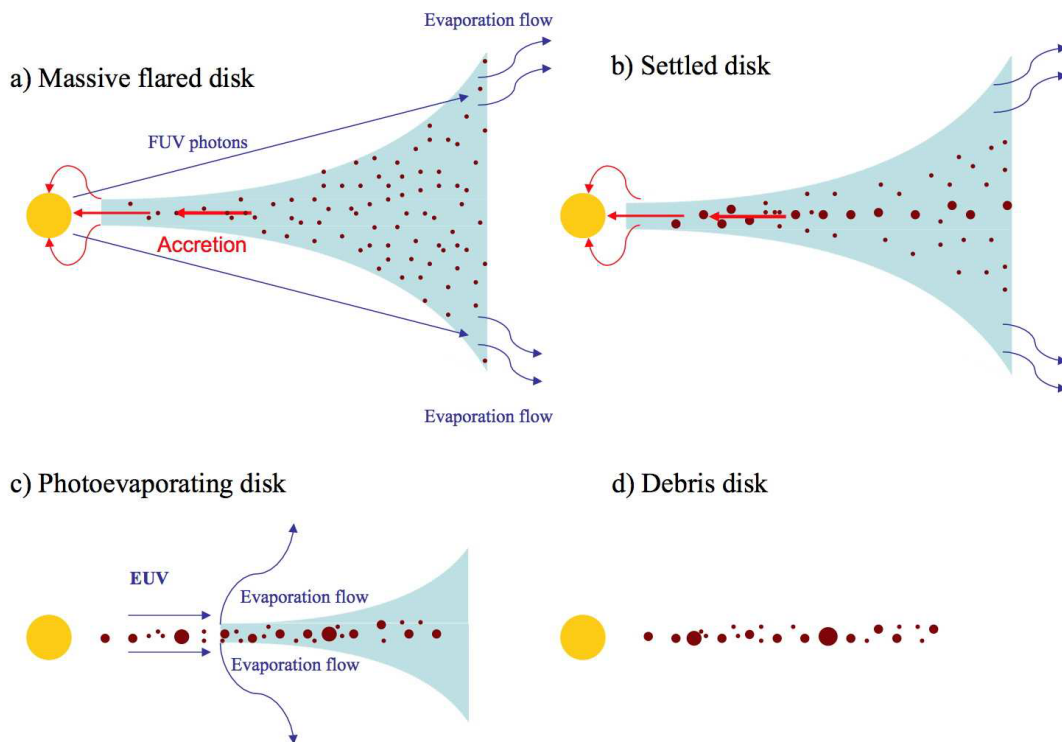
Figure 1: *The evolution of a typical circumstellar disk. The gas distribution is shown in blue and the dust in brown. (a) Accretion onto the star and FUV photoevaporation of the outer disk. (b) Grain growth into larger objects and settling in the mid-plane of the disk. (c) EUV photoevaporation becomes important; inner hole formation. (d) Remaining debris disk consisting of large grains and/or planets. (Figure taken from Williams & Cieza (2011).)*

The objects continue to grow through collisions and form protoplanets. According to the most accepted theory, the larger ones eventually start accreting gas, becoming giant planets with an

envelope of hydrogen and helium (Mordasini et al. 2010). Smaller planetesimals collide to form terrestrial planets. These new planetary systems go through more collisions, and eventually settle to a long-term stable configuration (Mordasini et al. 2010).

1.2   Methods of detection

There are currently just over 5000 exoplanets that have been confirmed (Christiansen 2022). However only two protoplanets have so far been detected with certainty, and they are PDS 70 b,c (Keppler et al. 2018; Haffert et al. 2019; Benisty et al. 2021).

A few more candidates have been reported, for example HD 100546 b,c, and HD 169142 b,c (Quanz et al. 2015; Currie et al. 2015; Biller et al. 2014), but their discoveries have been questioned by other researchers and methods (Thalmann et al. 2016; Ligi et al. 2018). Some candidates have also been reported but not yet confirmed, such as MWC 758 (Reggiani et al. 2018). Protoplanets have proven challenging to detect, as they are created in circumstellar disks with an abundance of dust and gas which outshines the planets and obscures a direct view. Young stars with possible protoplanets are also relatively far away, forcing us to take our current instruments to their limits in an attempt to directly see or infer one.

Different instruments and techniques have been used to try to detect protoplanets. Some of the methods used to observe many protoplanetary disks are direct imaging, sparse aperture masking (SAM) interferometry, deviations in Keplerian velocity patterns and angular differential imaging (Kraus et al. 2009; Willson et al. 2016; Benisty et al. 2022; Keppler et al. 2018; Pinte et al. 2018; Casassus et al. 2022). They are based on advanced instruments and complicated data reduction, making the process more difficult.

Current planet formation models predict that young planets are surrounded by circumplanetary disks from which they can accrete material (Lovelace et al. 2011). Other models explain that the planets can also accrete material from the circumstellar disks (Szulagyi & Ercolano 2020). Different models have predicted that protoplanets can emit in accretion tracers, like the H_α line, as a result of on-going accretion (Aoyama et al. 2021; Close et al. 2014). Current instrumentation allows us to test this hypothesis, using techniques like direct imaging in H_α filters with Adaptive Optics (AO) systems, or spectro-astrometry (Girard et al. 2020; Wagner et al. 2018).

In the following subsections we describe the spectro-astrometric (SA) method with two types of instruments, long-slit and integral field unit, which are used for our observations. SA is an observational technique that allows us to measure the relative position and extent of a source as a function of wavelength with extreme accuracy of milli-arcseconds (Bailey 1998).

1.2.1 Long-slit spectro-astrometry

Long-slit SA requires a standard slit spectrograph. Figure 2 is useful to follow the explanation of the concept. The slit output is a 2D spectra, the spatial axis (x) being parallel to the slit, and the spectral dispersion axis (λ_a) in the perpendicular direction (Mendigutía 2019). The spatial profile is extracted for each pixel along the dispersion direction, and a Gaussian function is fitted to determine the photocenter position (x_c) of the source as a function of the wavelength (Whelan & Garcia 2008). The position spectrum (x_c vs λ) shows shifts from the continuum spectrum of the star, which indicates the existence of non-symmetric structures like a binary companion, orbiting protoplanet or jets (Brannigan et al. 2006).
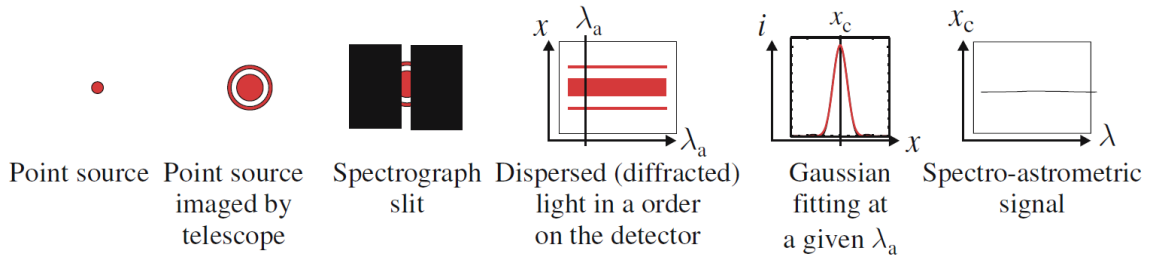

Figure 2: *Concept of long-slit SA applied to a single star source. See text for further explanation. (Adaptation of image from Whelan & Garcia (2008))*

Observations are done in two perpendicular directions so that we can infer the true direction of the source shift. Additionally, we observe sources with a parallel and antiparallel orientation for both directions. This is because instrumental effects can cause false SA signals which, unlike true signals, are not inverted between the two orientations (Whelan & Garcia 2008). In the end this means observations for each source should be done for 0°, 90°, 180° and 270°.

This method has been applied to observations of a wide variety of objects. For example, Baines et al. (2006) used long-slit SA to explore the binarity of Herbig Ae/Be star systems, demonstrating the technique for known binaries, and discovering a few new ones. Voigt & Wiedemann (2009) studied surface features of cool giant stars, calculated their size and temperature contrast from long-slit observations. Gnerucci et al. (2011) used the method to calculate the mass of a black hole from the rotating gas disk SA signal. More recently, the technique has been tested by Mendigutía et al. (2018) for its potential as an alternative to detect protoplanets around young stars.

1.2.2 IFU spectro-astrometry

If we want to obtain SA data over a certain area, it is possible to do so with the long-slit method by incrementally changing the slit position, but this is not very efficient as it requires taking many exposures. Another SA technique uses an Integral Field Unit (IFU), with which we can

observe an extended area. Figure 3 is useful with the following explanation of the concept. The instrument is made up of an array of microlenses, and light from each of them is then taken to the spectrograph using optical fibers. The output is a datacube with two spatial (x and y) and a spectral axis (λ). It can be viewed as a set of spaxels, spectra for each spatial point of the datacube. The logic of obtaining and analyzing the position spectrum of the source, as well as instrument artifact considerations, are the same as for the long-slit method and explained in the previous subsection.
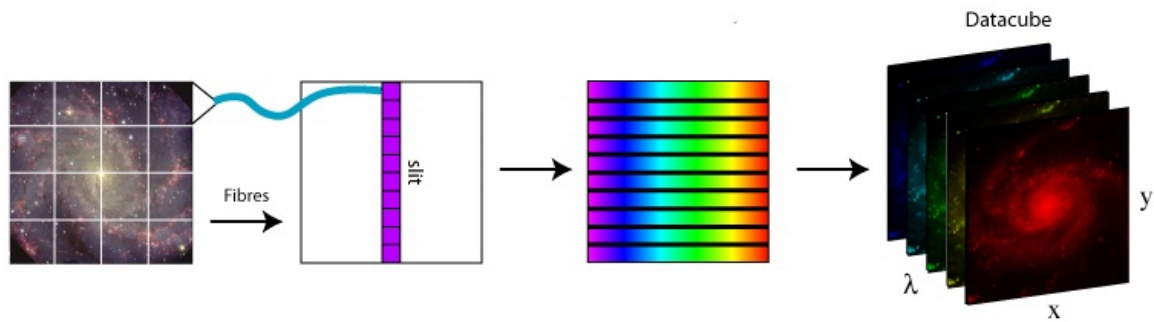

Figure 3: *Concept of IFU SA applied to a resolved extended source. See text for further explanation. (Adaptation of image by M. Westmoquette)*

IFUs have been previously used in different kinds of studies. For example, Garcia et al. (1999) showed the technique to be promising for use on pre-main sequence binaries, by studying a binary Z CMa with the OASIS IFU at the WHT. Whelan et al. (2006) explored outflow activity from low mass stars and brown dwarfs. Later, Whelan et al. (2015) tested the possibility of using the X-Shooter IFU to detect planetary companions of T Tauri stars. They conclude that an instrument with less complex data processing would be a better choice. Claudi et al. (2019) show that the technique is successful for obtaining better spectral and orbital characteristics of binary companions.

The Multi-Espectrógrafo en GTC de Alta Resolución para Astronomía (MEGARA) is an IFU at the 10.4 m Gran Telescopio de Canarias (GTC). The instrument was offered for research to the community at the end of 2018. It has not yet been used to perform SA on young stars, so we decided to test it for this purpose. One of the aims of this Master's thesis is to check its performance to understand if this is an optimal instrument to use the SA technique.

2 Observed targets

2.1 GU CMa

Also catalogued as HD 52721, GU CMa is a well known young Herbig Be eclipsing binary system. It has a binary separation of ∼0.65 arcsec, a position angle (PA) of ∼195° and its spectral type is B2Vn (Mendigutía 2019; Wheelwright et al. 2010; Shokry et al. 2018; Vieira et al. 2003).

We have observed GU CMa because of its well known SA signal. Previous works report a clear signal in both the photocenter and FWHM spectra, consistent with a binary system of similar brightness in the continuum but an H_α emission dominated by the central star (Mendigutía 2019). It is used here to demonstrate the long-slit method, and to test and compare with the performance of the MEGARA instrument.

2.2 LkCa 15

Located at a distance of ∼160 pc in the Taurus star-forming region, LkCa 15 is a young T Tauri star with spectral type K5 (Simon et al. 2000). It has a transitional circumstellar disk with a dust hole up to ∼46 au (Espaillat et al. 2007). Alencar et al. (2018) observed variability in the optical photometry of LkCa 15 and suggested that it might be caused by a misalignment between the inner and outer disks.

The first to report a possible discovery of a protoplanet orbiting LkCa 15 were Kraus & Ireland (2012), using non-redundant aperture masking (NRM) with NIRC2 at the Keck-II 10 m telescope for three observing runs in the span of a year. They presented observations of a candidate planet 'b' located at a separation of 72 mas. Sallum et al. (2015) later claimed a detection of three protoplanets ('b', 'c' and 'd') using NRM at the Large Binocular Telescope (LBT) (Figure 4). Using the Magellan Adaptive Optics System (MagAO), they also detected LkCa 15 b in H_α imaging observations, being the first accreting planet ever reported.

These detections were later questioned and tested by other techniques:

- Observations of LkCa 15 using J-band imaging polarimetry with the Spectro-polarimetric High-contrast Exoplanet REsearch (SPHERE) at ESO's Very Large Telescope (VLT) by Thalmann et al. (2016) show asymmetric structures in the inner disk at the location of the protoplanet candidates. They conclude that this could explain the SAM signal previously assigned to the candidates, however they could not disregard LkCa15 b due to the separate observation in H_α.
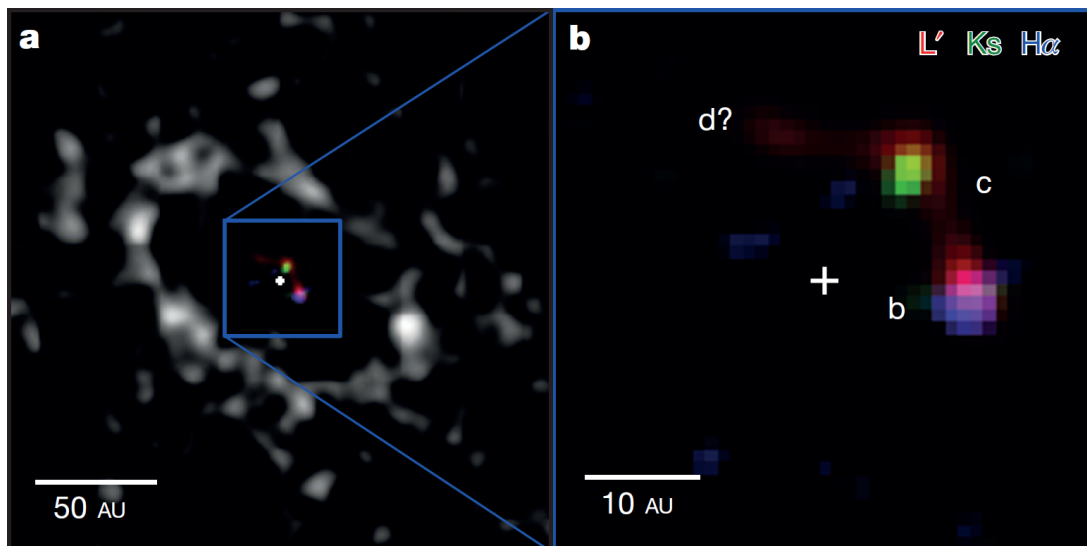
Figure 4: *Observations of candidate planets 'b', 'c' and 'd' reported in Sallum et al. (2015).* **a:** *Composite H$_\alpha$ (blue), Ks (green), and L (red) image from LBT and Magellan, overlayed on VLA millimetre observations (greyscale) observed by Isella et al. (2014).* **b:** *Closer view at the composite image from LBT and Magellan with candidate planets b, c, and d marked. Figure adopted from Sallum et al. (2015).*

- Mendigutía et al. (2018) performed long-slit SA observations of LkCa 15 in H$_\alpha$ using the ISIS spectrograph at the 4.2 m William Herschel Telescope (WHT) and did not detect the predicted photocenter shift for LkCa 15 b. They do find a broader FWHM signal suggesting an extended H$_\alpha$ emission, possibly caused by variable disk wind. Note that in an earlier work, Whelan et al. (2015) used SA data obtained with X-Shooter on the VLT to study the presence of LkCa 15b. However, they conclude that the instrument was not well suited for this kind of observations.

- Currie et al. (2019) came to a similar conclusion as Mendigutía et al. (2018) using near-infrared direct imaging/spectroscopy from the Subaru Coronagraphic Extreme Adaptive Optics (SCExAO) system with the CHARIS IFU and multi-epoch imaging from Keck/NIRC2. Similarly, Blakely et al. (2022) show that an extended disk structure fits the observations better than the proposed protoplanets, this time using SPHERE at the VLT.

Since previous studies are not yet conclusive on the nature of the LkCa 15 system, it is a good target to observe with different instruments and techniques. SA has already been used to observe stellar systems with possible companions. One of the aims of our observations is therefore to test if the MEGARA instrument at the GTC can reach the needed precision to detect potential accreting protoplanets around LkCa 15.

3   Observational data

In this section we present details of the instruments and the obtained data, first for the long-slit (3.1) and then for the IFU observations (3.2). The previously explained SA methods will be demonstrated through the reduction process explained in subsections 3.3 and 3.4.

3.1   Long-slit observations

Long-slit observations were made with the Intermediate-dispersion Spectrograph and Imaging System (ISIS) at the 4.2 m William Herschel Telescope (WHT) in the La Palma Observatory. We used RED+, a detector array on the ISIS red arm, which consists of 2048 × 4096 (15.0 micron) pixels. The dispersion element we chose was a R1200R grating centered on H_α, with a wavelength range of 5991-9531Å and a spectral resolution of 9333.

GU CMa

Object frames of GU CMa were taken on 5 January 2018 in two perpendicular directions. For each direction two frames were observed, rotated 180° relative to each other. The PA of the observations are 13° and 193° in the parallel, and 103° and 283° in the perpendicular direction. Note that the PA is measured relative to the north celestial pole, turning in the positive (counterclockwise) direction.

3.2   IFU observations

IFU SA observations were done using the MEGARA instrument at the 10.4 m Gran Telescopio Canarias (GTC). Its IFU is the Large Compact Bundle (LCB), which covers an area of 12.5 arcsec × 11.3 arcsec with 567 fibres and has a spaxel size of 0.62 arcsec. It has 56 additional fibres at the edge of the field for sky subtraction, meaning there is a total of 623 fibres on the LCB spectrograph pseudo-slit. The dispersion elements of the MEGARA IFU are Volume Phase Holographic (VPH) gratings. We used the HR-R grating which provides a resolving power of 20050 in the wavelength range 6405.61 - 6797.14Å, centered on 6602.59Å, for our observations which are focused on H_α.

GU CMa

The binary GU CMa was observed with MEGARA by its team in 2019 to test its SA capabilities, as GU CMa has a well known SA signal. Observations were done at PA of 0° and 50° to be able to check for possible instrumental effects. Unfortunately, the data taken at 0° was centered on the wrong target, so we will reduce and analyze only one set of data. The standard star HR3454 was observed on the same night and with the same instrumental setup for calibration purposes.

LkCa 15

As part of a pilot program for testing the SA capabilities of MEGARA, LkCa 15 was observed in December 2020 in visitor mode, but the weather conditions were too poor for a comprehensive analysis of the signal. For more details, please see Appendix A. That is why observations of LkCa 15 were repeated in February 2022 in service mode under better atmospheric conditions, which is the data we have analysed in this work.

Data was obtained on a clear night for PA of 0° and 180°. The required seeing was set at ≤1.2", and the values provided by the observatory for observations at the two angles were 1.1" and 1.0" respectively. We obtained 6 individual spectra of 600 seconds each for each PA. The standard stars HR153 and HR5501 were also observed during the same night for the calibration.

Basic information about each observation is shown below in Table 1.

Table 1: *Summary of observations*

Instrument	Object	Obs. date	Exposure time [s]	# of exp per angle	# of angles	Airmass
WHT/ISIS	GU CMa	05.01.2018	(3x25s)+(1x10s)	1	4	1.31-1.32
GTC/MEGARA	GU CMa	27.02.2019	20	16	1	1.47-1.57
GTC/MEGARA	LkCa 15	05.02.2022	600	6	2	1.04-1.40

3.3   WHT/ISIS data reduction

Long-slit data reduction was done with IRAF, an Image Reduction and Analysis Facility from the National Optical Astronomy Observatory (NOAO). Publicly available user guides and manuals [1] were followed for each step of the reduction to derive the intensity flux as a function of wavelength in the slit direction. This is followed by the SA reduction in the spatial (perpendicular) direction, as will be described.

First, bias subtraction was performed, a standard starting point of the reduction procedure for CCD imaging and spectroscopy. Its purpose is to correct for the electronic offset on each pixel, added to avoid negative values at detector readout. These calibration images are taken with 0 seconds exposure time, to only capture the electronic offset. The task *zerocombine* takes all bias files and creates a master bias. The subtraction of the master bias from all other calibration and object images is done using the *ccdproc* task.

The next step is the flat field correction. It is based on homogeneously illuminated calibration images, which allow us to correct for sensitivity variation between pixels of the detector. A master flat image is created as an average using the *flatcombine* task, and then normalized with

---

[1] https://iraf-community.github.io/doc/beguide.pdf
http://212.193.72.50/docs/iraf/ccduser.pdf
https://noirlab.edu/science/sites/default/files/media/archives/documents/scidoc0479.pdf

the *response* task by fitting an order 12 polynomial. The flat field correction is also part of the *ccdproc* task, dividing all other images by the normalized master flat.

After these corrections, the spectrum needs to be extracted, meaning that the counts per second for each pixel in the dispersion axis have to be obtained. The problem is that the spectrum is not perfectly aligned with the dispersion axis because of camera distortions, position of the dispersion grating or differential atmospheric refraction (an effect discussed and corrected for in section 3.4). Because of this, after finding the strongest peak along the spatial axis and defining an extraction window, the profile center is traced as a function of the dispersion axis. Using interactive fitting of different functions and orders, the spline3 function of order 12 was chosen for extracting the spectrum. Aperture extraction and trace fitting was done using the *apall* task. After the spectrum has been extracted in the dispersion axis, the spatial axis can be studied next.

The position spectrum was derived using the task *fitprofs*. For each pixel in the dispersion axis it fits a Gaussian described by a center and FWHM. These values characterize the photocenter and physical extent of the observed system, which includes the effects of seeing and instrumental broadening. For short wavelength ranges this broadening is assumed to be constant, so the variations are considered to occur due to changes in the emitting region itself. The result is a text file for each object image, containing positions of the photocenters and the FWHM as a function of pixels in the dispersion axis, which are converted into wavelength units as follows.

Wavelength calibration was done by first extracting apertures for lamp files, comparison exposures of Cu-Ar-Ne lamps with a well known spectrum, using the same aperture and trace as for the object files. Lines in the lamp spectra were identified by comparing with expected spectral lines from the manual using the *identify* and *reidentify* tasks. These solutions were then applied to the object files.

3.4   GTC/MEGARA data reduction

The data from GTC/MEGARA was reduced with the MEGARA pipeline, which was developed by the MEGARA team. Their Data Reduction Cookbook [2] was followed for all steps of the reduction process.

The first step was the bias subtraction, performed using the *Bias* recipe on all other calibration and object images. Like previously described for long-slit reduction, bias calibration images are taken with 0 seconds of exposure time to correct for electronic offset of the detector.

This step is followed by making a 'trace map' in order to identify the position of each fiber in the detector, using a set of flat-field images. These images were obtained using a

---

[2]http://www.gtc.iac.es/instruments/megara/media/MEGARA_cookbook_1H.pdf

continuum halogen lamp which provides homogeneous illumination of the fibers. Using the megaradrp-overplot recipe, the traces were overplotted onto the reduced image to check that the fibers are correctly identified, and validate the Trace Map. The positions of the fiber traces at the detector can be shifted due to a change in the ambient temperature. This can be the case when the flat-field images and the scientific target exposures are obtained at different times, in which case they need to be corrected.

The same set of flat-field images is processed again to create a model map using *ModelMap* recipe. The goal of this step is to estimate the fiber profiles: first, the central position of each fiber is estimated using the 'Trace map'. Then, the profiles are fitted for every 100 columns with a Gaussian function extracting the central position and sigma. Finally, the profiles are interpolated for each column using splines. As a byproduct of the reduction process, the extracted values of Gaussian center and sigma were plotted for each fiber, and were found to be within the expected values, according to the MEGARA manual.

The wavelength calibration of each fiber was done using *MegaraArcCalibration* recipe, and arc-lamp frames from the ThNe hollow-cathode lamp were used. Intermediate files were checked to make sure enough lines were recognized and used for the fit. Before running the recipe, the traces were overplotted on the raw arc frames to check that they were well aligned. If not, an adequate offset should be applied.

Since each optical fiber is a separate optical system, their light transmission and wavelength dependence vary. This was corrected once again with fiber-flat continuum lamp images, using the recipe *MegaraFiberFlatImage*.

The flux calibration of the data can be done using standard stars observed during the night with the same instrumental setup as the scientific observations. In our case, an absolute calibration is not needed. However, to get familiar with the procedure, we have used the standard star observations of the night to derive a sensitivity curve, and to perform a relative flux calibration using the average atmospheric extinction curve provided by the observatory.

Using all the previously described calibrations, the scientific observations were reduced with the recipe *MegaraLcbImage*. During the procedure, the sky was also subtracted by combining 56 fibers which were dedicated to this task. The final reduced sky-subtracted data is saved in a Row-Stacked Spectrum (RSS) 2D image, including all of the 623 fiber spectra.

The megara-qla software was used to visualize the reduced data, and to extract the spectrum. Figure 5 shows the software interface featuring three main panels. We extract the spectrum from the central spaxel and two surrounding rings, as seen in the Focal Plane panel. The selected fibers are highlighted in the RSS panel, and their spectrum is shown in the Spectral panel. The spectrum is saved to a text file to be used later for the analysis.
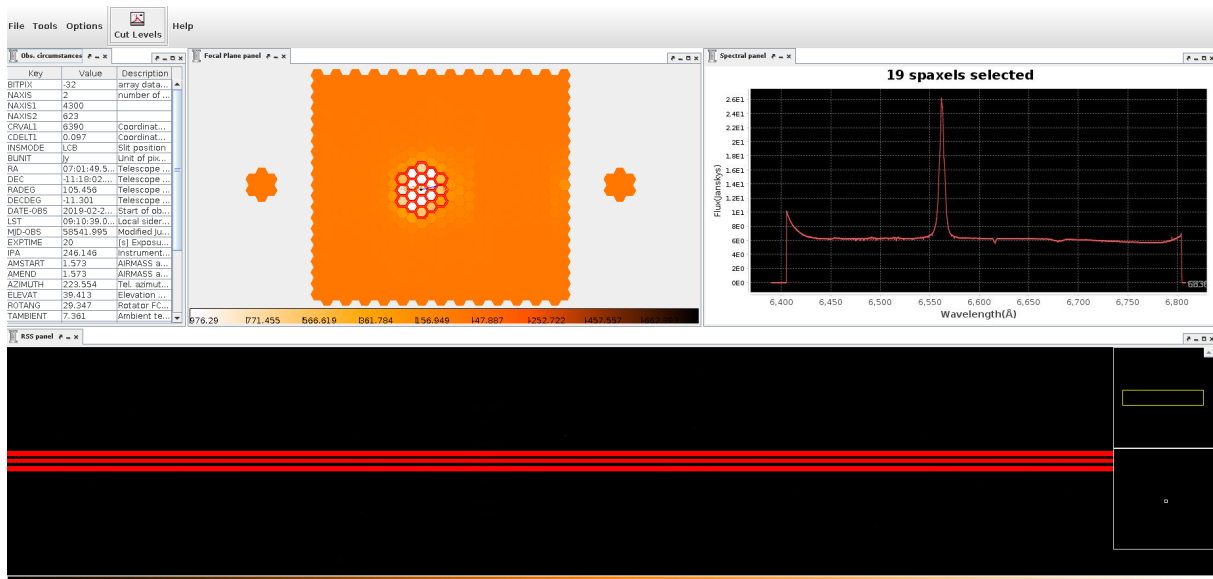
Figure 5: *Megara-qla software, developed by the MEGARA team and used for visualizing the reduced data and extracting the spectrum. The main panels are the reconstructed RSS images (top left), the spectrum at the selected spaxels (top right), and the RSS panel (bottom). The example shows the reconstructed image of GU CMa, and the spectrum in the central spaxel and two surrounding rings (red hexagons marked in the reconstructed image).*

As part of the reduction process, the tool *megaradrp-cube* was used to convert the fully reduced RSS file into a FITS data cube. A plate scale of 0.3 arcsec/pix and a linear interpolation method were used. The data cube has two spatial dimensions, with 43 and 40 pixels in the X and Y directions respectively. The third is the spectral dimension and consists of 4300 slices. DS9 was used for visualizing the data cube to check the quality of the final result and to identify problems that could occur during the reduction process.

4 Analysis and results

In this section we will show and discuss first the long-slit and then the MEGARA results. The observed signals will be explained and compared with previously published work.

4.1 WHT/ISIS data analysis and results

For the long-slit observations of GU CMa we show the intensity spectrum for both pairs of slit PA in the top panels of Figures 6 and 7. Normalization was done by fitting the continuum and dividing the spectrum by it, which sets it at unity. The spectra were averaged between the two mutually parallel slit positions to improve the signal to noise ratio (SNR).

The photocenter and FWHM spectra were also derived and plotted in the middle and bottom panels of Figures 6 and 7. A spatial scale of 220 mas/pixel was used to translate the y-axes from pixels to an angular scale for both spectra. Finally, a continuum subtraction and normalization of photocenter and FWHM plots was done. The continuum spectrum was fitted to a polynomial, making sure to chose parts of the background and avoid spectral features, and was then subtracted. It is assumed that the continuum spectrum predominantly comes from the central star. The idea of this normalization is to set that as the zero-level, so the FWHM signal is interpreted relative to it. The photocenter spectra for both parallel orientations of each pair are represented with lines of different color. If there were any instrument errors, they would remain the same regardless of the angle, whereas true signals are always reversed between the two slit positions. This can be seen clearly in Figure 6, where we observe a strong photocenter shift. Both the photocenter and FWHM spectra for the parallel orientations contain clear peaks at H_α, signifying the existence of an object orbiting the main star. For the perpendicular direction we notice from Figure 7 that the photocenter shift is not visible, and the change in FWHM is much smaller. This suggests that the plane of the main star and nearby object is more aligned with the parallel than the perpendicular slit direction.

The described SA results for GU CMa are consistent with the presence of a companion located at a PA of $\sim$198°. Previous SA studies report similar results (Wheelwright et al. 2010; Mendigutía et al. 2018).

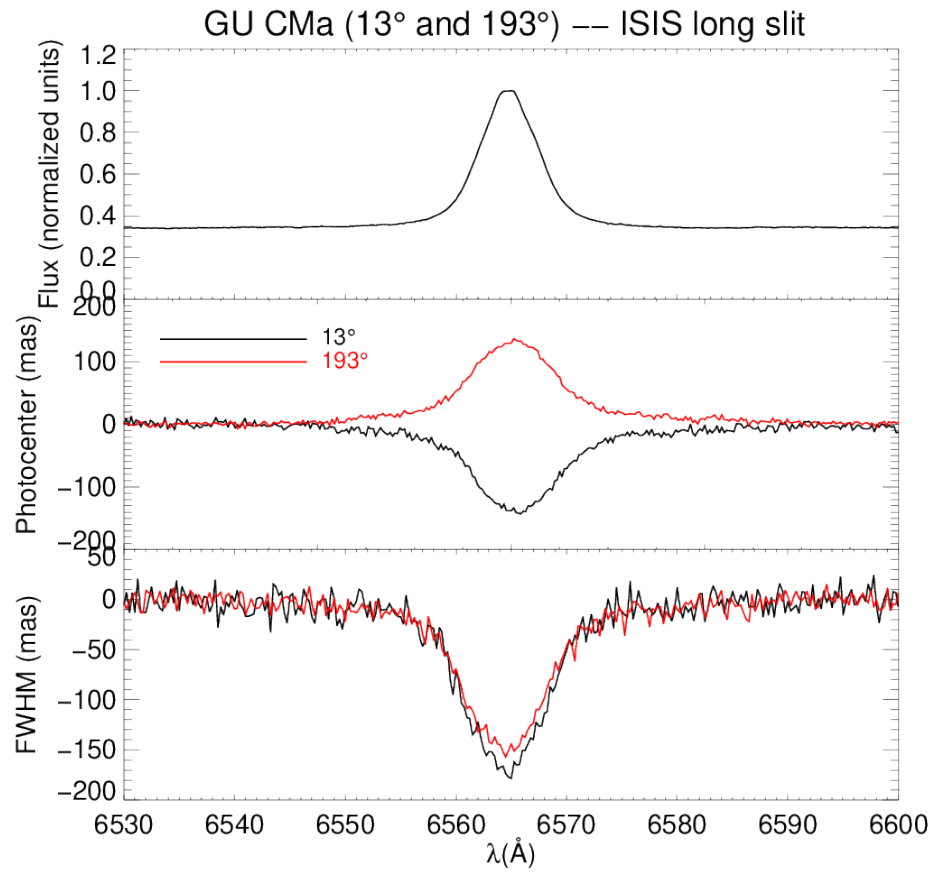**Figure 6:** *The top panel shows the intensity spectrum in a wavelength range centered on H_α. In the middle and bottom panels the photocenter and FWHM spectra are plotted for both the 13° (black line) and 193° slit positions (red line). Each of the two shows a clear SA signal at H_α.*
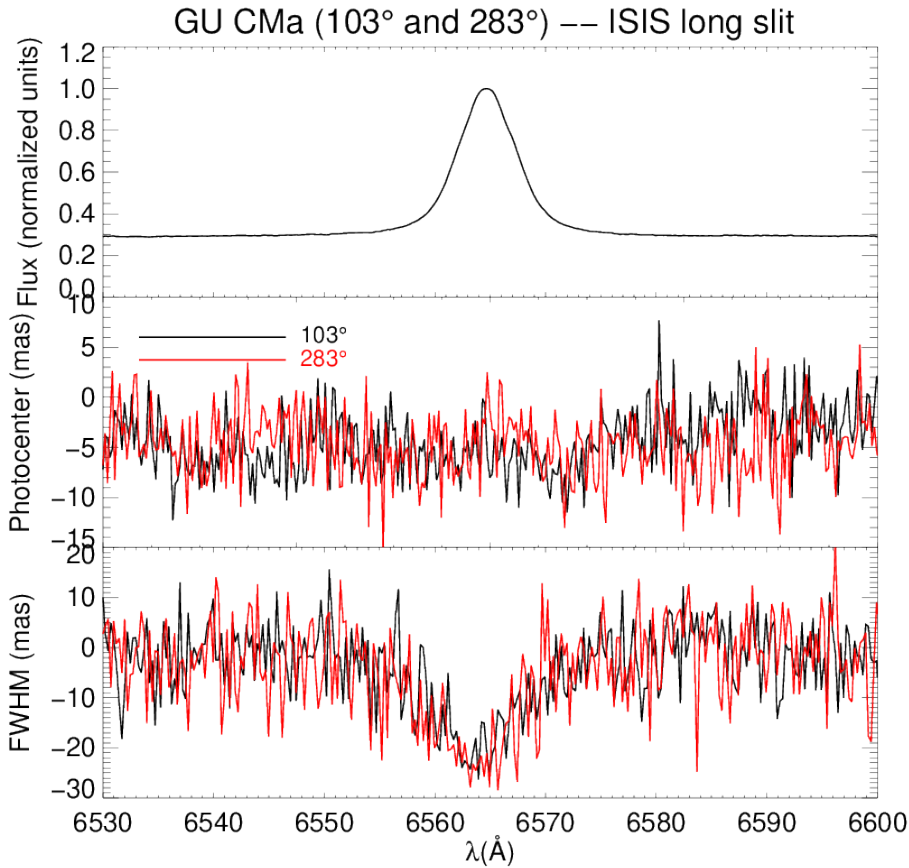
Figure 7: *The top panel shows the intensity spectrum in a wavelength range centered on H_α. In the middle and bottom panels the photocenter and FWHM spectra are plotted for both the 103° (black line) and 283° slit positions (red line). We don't observe a photocenter shift at H_α, and the FWHM signal is smaller than in the other slit positions.*

4.2 GTC/MEGARA data analysis and results

The analysis of the final reduced data was done with a customary code written with the Interactive Data Language (IDL). As a first step, it takes the previously mentioned datacube and fits 2D Gaussian functions to each individual plane, so that the centroids and FWHM of the stellar target are derived for each wavelength.

For each object we observe that the centroids are visibly displaced due to the effect of differential atmospheric refraction (DAR), as will be clearly seen in Figures 8, 13, 14. This effect of light refraction occurs because of the Earth's atmosphere, causing objects to appear closer to the zenith than they actually are. The extent of the shift also depends on wavelength, as shorter wavelengths are refracted more than longer ones. The DAR effect and corrections are explained in more detail in Menezes et al. (2014), Arribas et al. (1999), and Stomski et al.

(2003). It is an active effect because it changes with time as the zenith angle changes, and needs to be corrected accordingly. The DAR effect is also seen in other IFU observations with instruments that are not equipped with an Atmospheric Dispersion Corrector (ADC), as reported in Garcia et al. (1999) and Menezes et al. (2014). In our case, a correction was done by fitting polynomials of the second order to the centroids, separately for both the x and y direction. Polynomials of higher order did not significantly improve the correction, for example changing the standard deviation from 1.8952 mas to 1.8938 mas in the case of LkCa 15 at 0°, so only the second order was used. The DAR corrected photocenters and values of FWHM, in addition to the stellar spectrum, were then plotted as a function of wavelength.

In most of the plots of intensity, photocenters and FWHM for all the observed objects (Figures 11, 16, 17), there is a signal at 6618 Å. This is an artifact related with a ghost coming from the zero-order dispersion [3].

In the following subsections, we show the main results obtained for each of the targets observed with MEGARA.

4.2.1 GU CMa results

GU CMa data was reduced following the MEGARA manual as described above. No shifts were observed when overplotting the traces, so corrections weren't needed for this data. The star HR3454, observed on the same night with the same instrumental setup, was used to derive the sensitivity curve and perform the flux calibration.

The previously described DAR effect can be clearly seen in Figure 8 (left) as a dispersion of photocenters in the X and Y directions around 0. This dispersion depends on wavelength, which is shown by a colorbar accross the full observed spectral range of 6450 - 6660Å. A clear shift in photocenter position is seen at H_α even before the correction of the DAR. The fits of photocenters in the X and Y directions separately, are shown in Figure 8 (right) as red lines. Note that the region around H_α, in which we are interested, was excluded from the fitting. The fits are used to derive the final corrected photocenter plot (Figure 9). The photocenters are now centered on 0, and we calculate a shift of $\sim$139 mas at H_α. Observations taken in 2002. reported by Baines et al. (2006) show a photocenter shift of $\sim$132 mas, which is comparable with our results. More recently however, Mendigutía et al. (2018) finds a shift of $\sim$189 mas. These differences in the reported shifts can be attributed to the variability of the source, meaning the relative intensity of the two stars can vary and therefore affect the shift observed in the H_α line. From the photocenter shift we calculate a PA of $\sim$197°, which is consistent with previously reported results by Wheelwright et al. (2010) and Mendigutía et al. (2018). Figure 10 shows the photocenter plot that has been rotated for a clearer comparison with the SA signal of GU CMa, as reported by Wheelwright et al. (2010).

---

[3]For more details see http://www.gtc.iac.es/instruments/megara/megara.php#First_sight_on_data
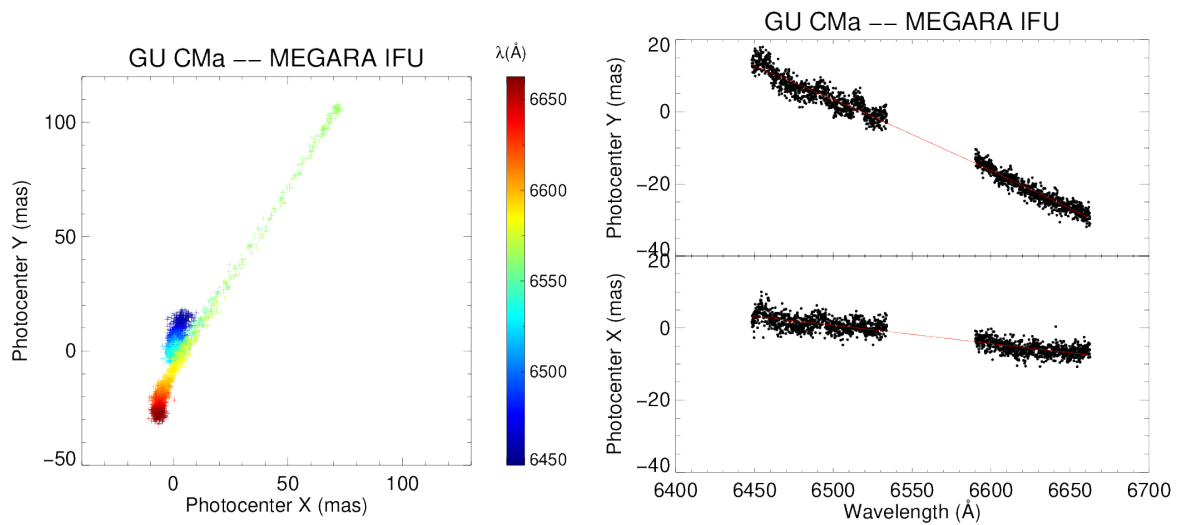
Figure 8: *Left: Photocenters are plotted in the X and Y direction for the GU CMa data. The colorbar shows the relation with wavelengths in the range of 6450 - 6660Å. The dispersion of the photocenters around 0 is caused by the DAR effect. Right: To correct for the DAR effect, polynomials were fitted to the data in the X and Y direction separately. The region which we are interested in around H_α was excluded for the fit (shown with a red line).*

The top panel of Figure 11 shows the intensity spectrum of GU CMa. In the other two panels, the photocenter and FWHM spectra are plotted for both the X and Y directions, with a clear SA signal seen in both. The average SA precision, the standard deviation of the signal outside the H_α line in the range 6510-6550 Å, is $\sim$2 mas.
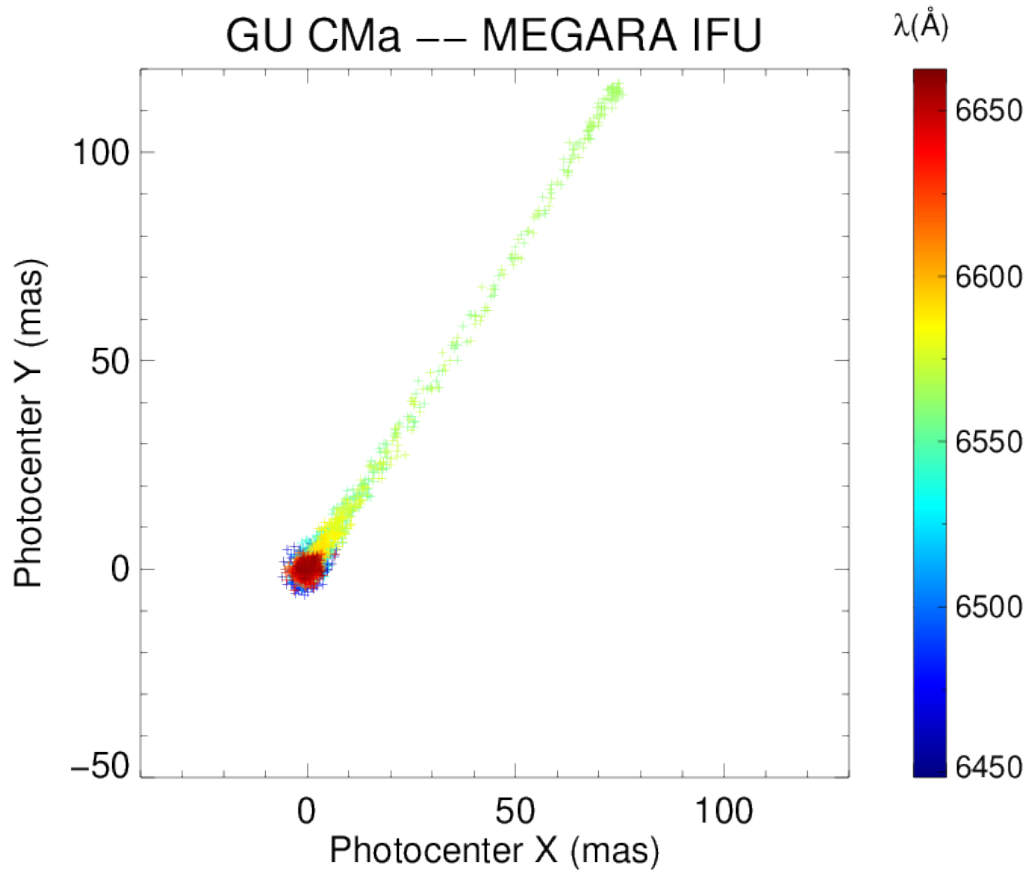
Figure 9: *Photocenters are again plotted in the X and Y direction for the GU CMa data, this time after applying the DAR correction. The colorbar shows the full range of wavelengths. The data is now centered on 0, with a clear shift at H_α.*
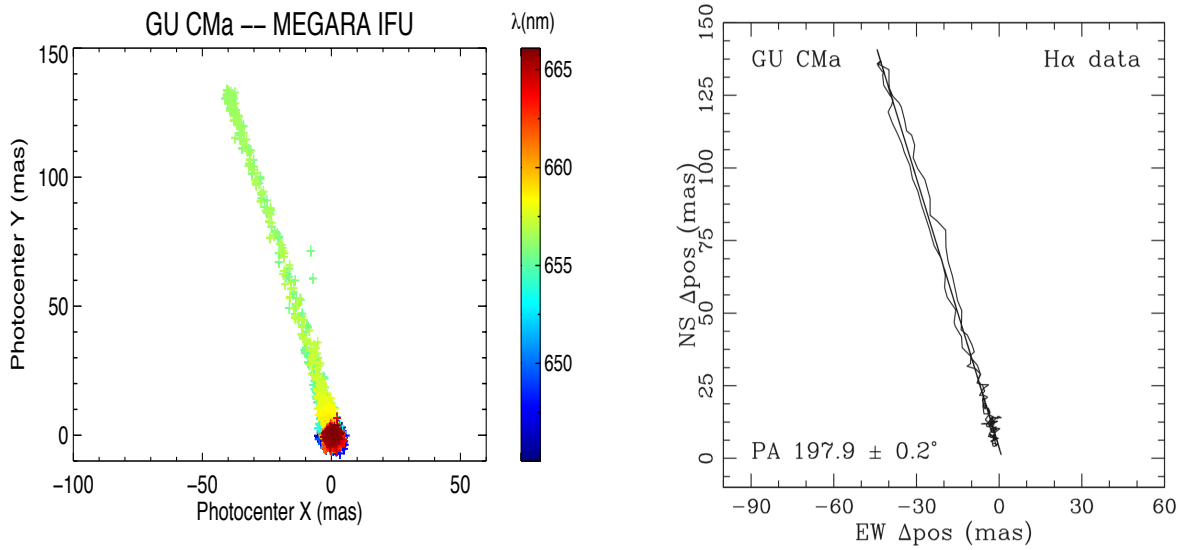
Figure 10: *Left: H_α SA signal detected in the Herbig Be star GU CMa with MEGARA IFU. The signal is consistent with a binary companion at PA of 197.9°. Right: For comparison, we include the similar H_α SA signal detected in the same target by Wheelwright et al. (2010).*
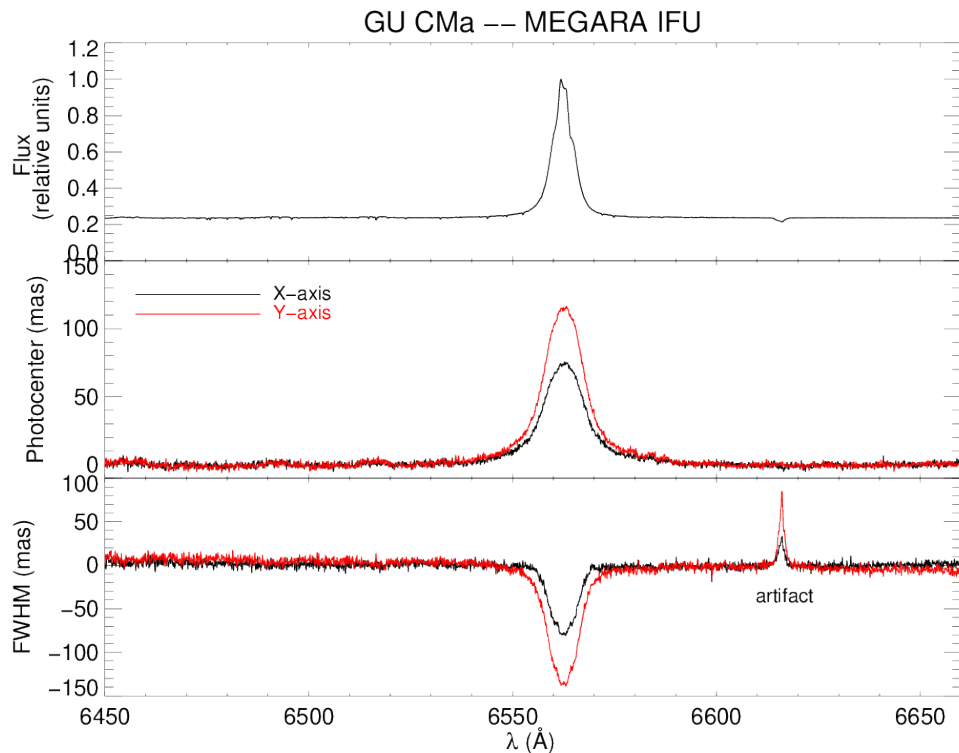

Figure 11: *The top panel shows the intensity spectrum in the observed wavelength range of 6450 - 6660Å. In the middle and bottom panels the photocenter and FWHM spectra are plotted for both the X (black line) and Y direction (red line). Each of the two shows a clear SA signal at H_α, while in the intensity and FWHM spectra we also notice the instrumental artifact around 6618Å.*

4.2.2 LkCa 15 results

In the case of LkCa 15, a shift of 3 pixels was observed between the science frames and Trace Map. This was corrected during the reduction process with a 3 pixel offset and checked by overplotting. The standard star HR153, which was observed during the same night as LkCa 15, was used in the flux calibration procedure.

The DAR effect is very pronounced in the LkCa 15 data, with a significant change of direction for the observation at 0° (Figure 12). In the area nearby H_α the fit is fairly linear, so we take this range for fitting and further analysis. This is not a problem since we are interested specifically in the SA signal at H_α. The effect and XY fits in the chosen range of 6450 - 6660Å are shown in Figures 13 and 14 for 0° and 180° respectively. After the correction, the photocenters in the X and Y direction are presented in Figure 15, now centered on 0.
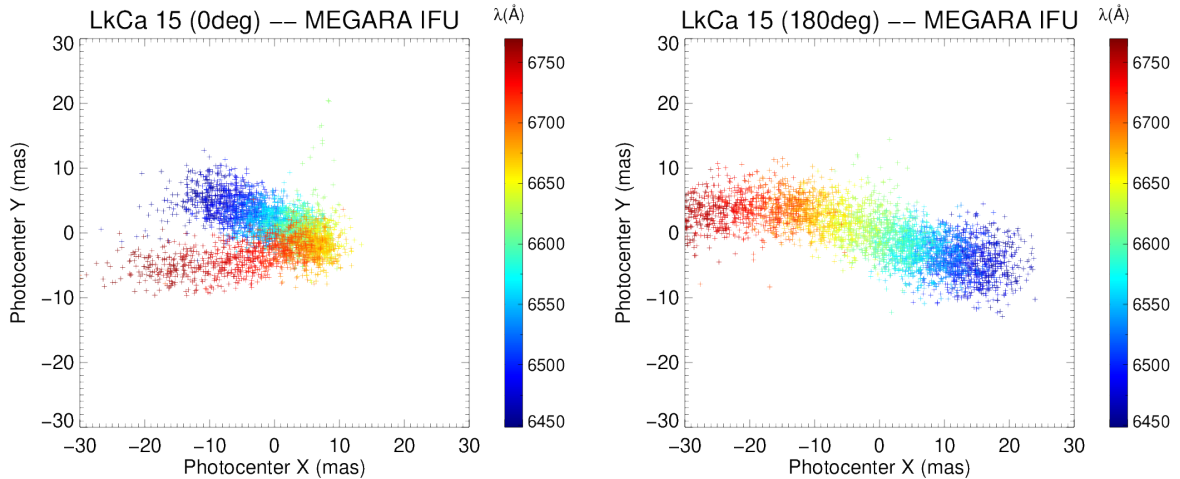

Figure 12: *DAR effect shown for the entire spectrum range of the observed LkCa 15 data at 0° (left) and 180° (right). The full data can not be linearly fitted, so we chose only the range of interest nearby H_α for the correction and analysis.*

The top panels of Figures 16 and 17 show the intensity spectrum of LkCa 15 for 0° and 180°. We see a two peak profile of the H_α line, with the one at a shorter wavelength being stronger. The middle and bottom panels show the photocenter and FWHM spectra, respectively, with the X-axis data plotted in black and Y-axis data in red.
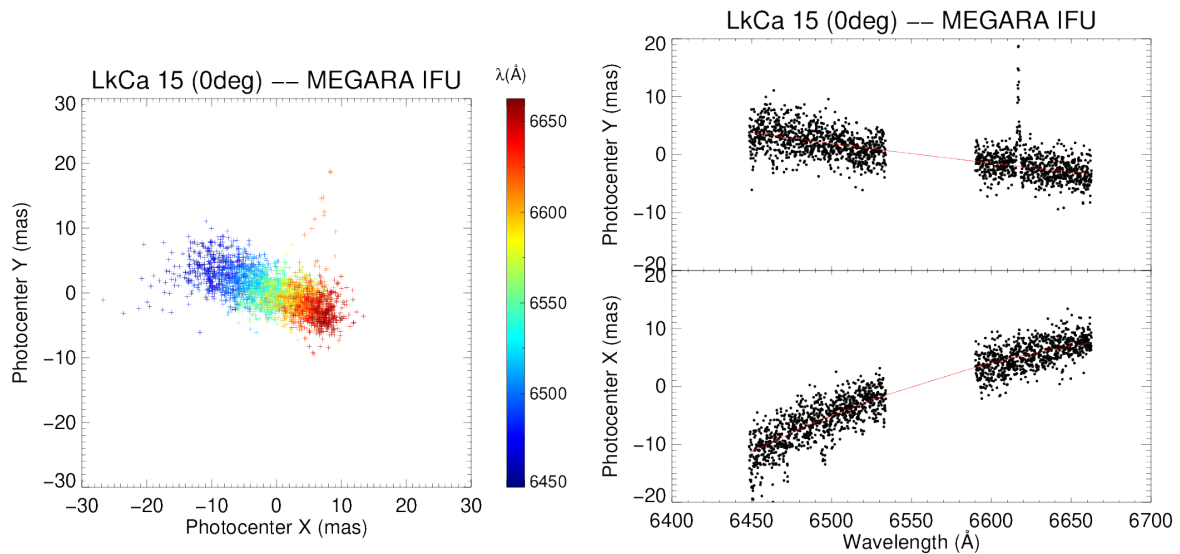
Figure 13: *Left: Photocenters as a function of wavelength, showing the DAR effect and no shift at H_α for LkCa 15 observet at PA 0°. Right: Fitting of the photocenters in both the X and Y directions for the DAR correction, avoiding the wavelength range around H_α.*
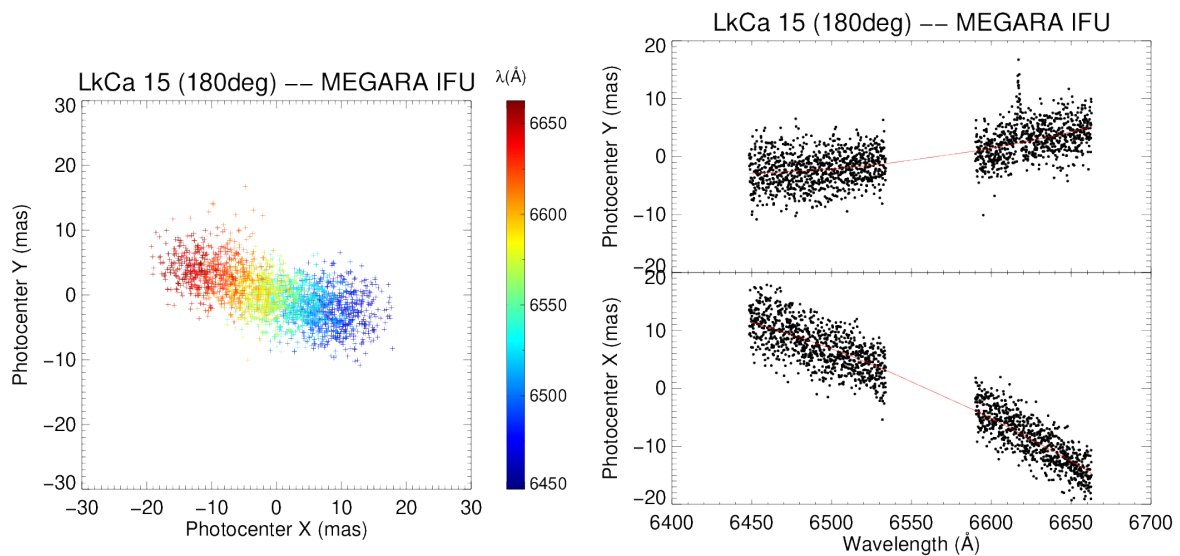

Figure 14: *Left: Photocenters as a function of wavelength, showing the DAR effect and no shift at H_α for LkCa 15 observed at PA 180°. Right: Fitting of the photocenters in both the X and Y directions for the DAR correction, avoiding the wavelength range around H_α.*
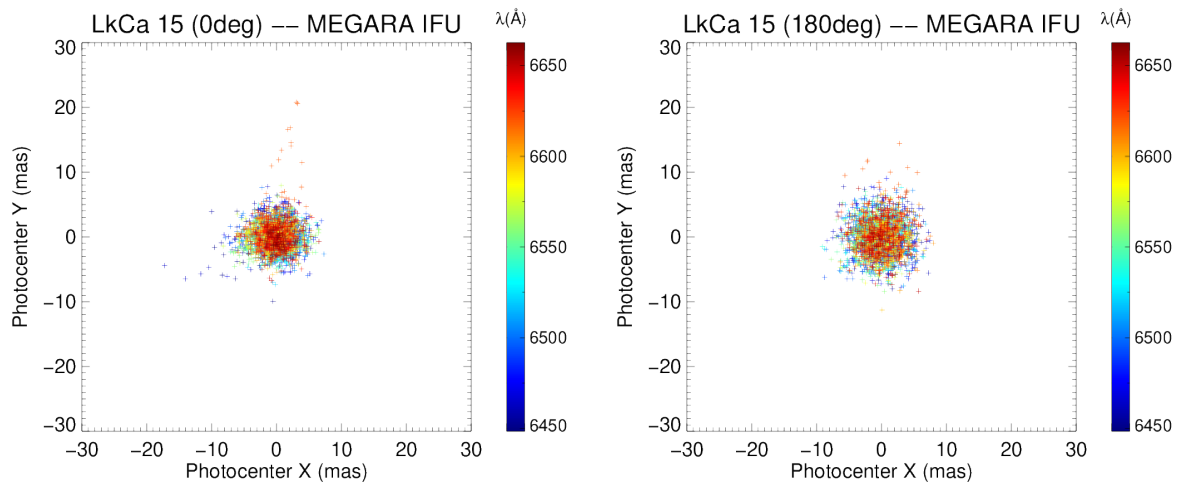
Figure 15: *Photocenters after performing the DAR correction on LkCa 15 data at 0° (left) and 180° (right).*
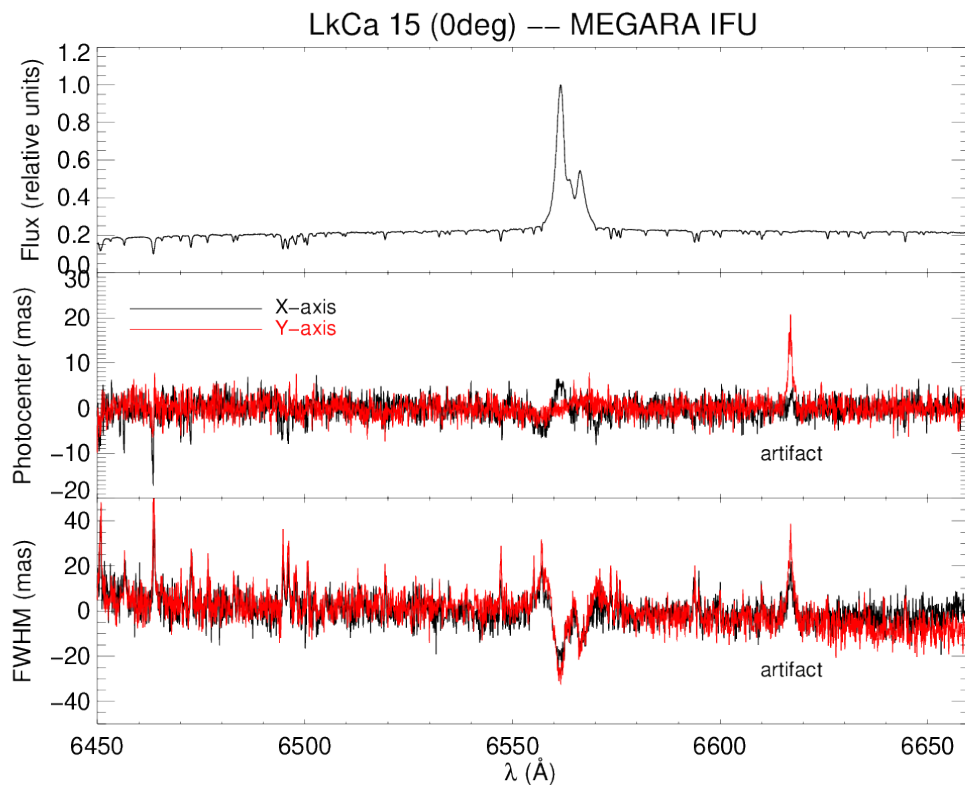

Figure 16: *Plots showing the intensity, photocenters and FWHM as functions of wavelength for LkCa 15 at 0°.*
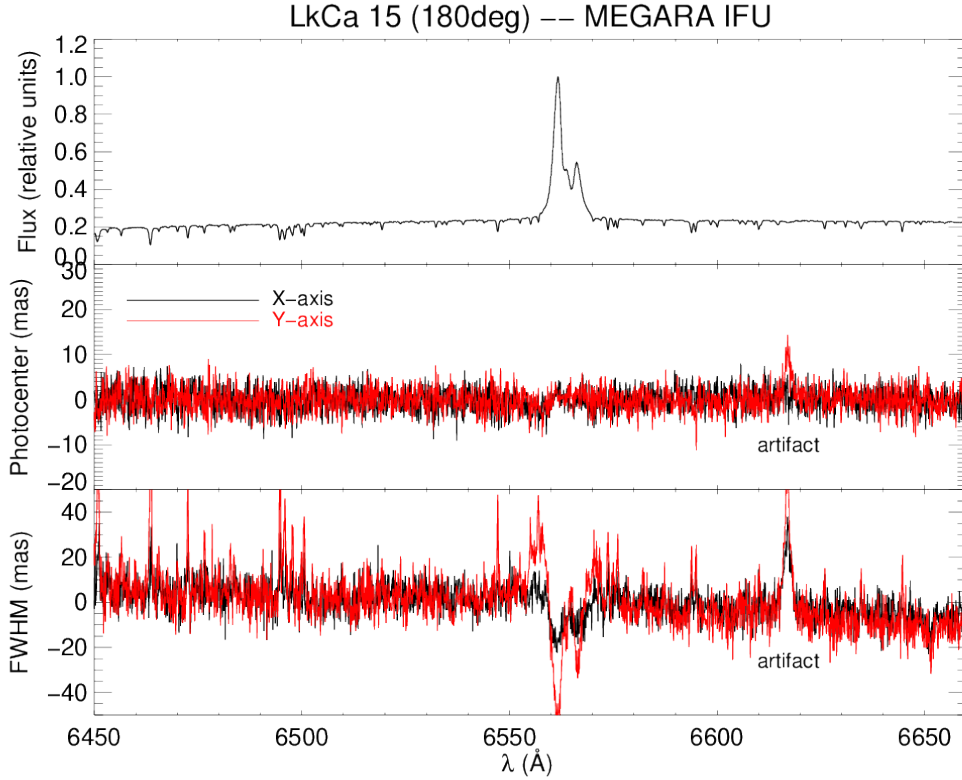
Figure 17: *Plots showing the intensity, photocenters and FWHM as functions of wavelength for LkCa 15 at 180°.*

Focusing first on the photocenters, we observe a SA signal in the H_α line for the datasets in both angles. The measured SA precision of the datasets outside the H_α line is $\sim$2.0 mas for 0° in the X and Y directions, and $\sim$2.7 mas for 180°. For a clearer view of the SA signal, we show a comparison of data for the two angles centered on H_α (Figure 18). The top panels show the intensity spectrum for LkCa 15, while the middle and bottom panels show the photocenters in the X and Y directions. The expected SA signal from Sallum et al. (2015) for an accreting planet is $\sim$0.8 mas, based on the reported 93 mas separation and 5.2 mag contrast in H_α. It's calculated using the equation 4.1, where s is the separation in mas and $c_{H\alpha}$ is the contrast in magnitudes in H_α (Mendigutía 2019).

$$\delta = \frac{s}{10^{0.4c_{H\alpha}} + 1} \tag{4.1}$$

In order to reach the wanted SA precision for planet detection, we reduced the dispersion by applying an aggressive binning to our data (with 20 values being averaged) while still showing two peaks in the intensity spectrum. The improved SA precision is $\sim$0.6 mas for both angles in the X and Y directions, which would be enough to detect the proposed planet. We detect a SA signal at H_α that varies in intensity between the two angles, while keeping the same shape

in both X and Y directions, instead of being inverted. This means the signal we observe is more likely an artifact, and we need to investigate its origin. From this data we can't conclude anything about a possible planet, as its signal could be embedded in the signal caused by the artifact.
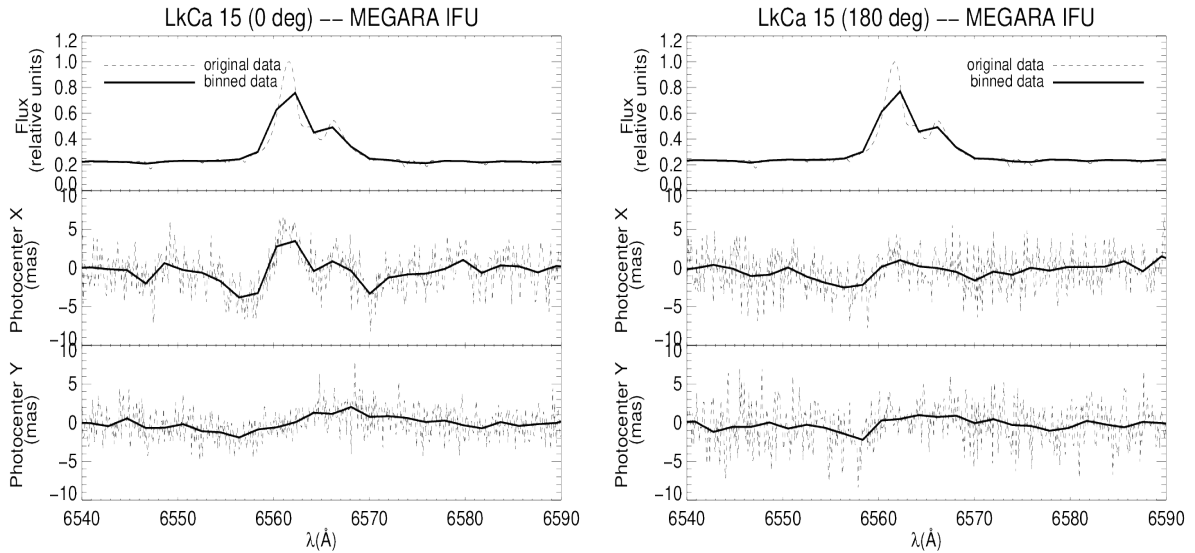

Figure 18: *Top panels show the intensity spectrum. The middle and bottom panels show the photocenter displacement in XY-directions, respectively, centered on the H_α line for observations of LkCa 15 at 0° (left) and 180° (right). Original (dashed) and binned data (full line) are plotted.*
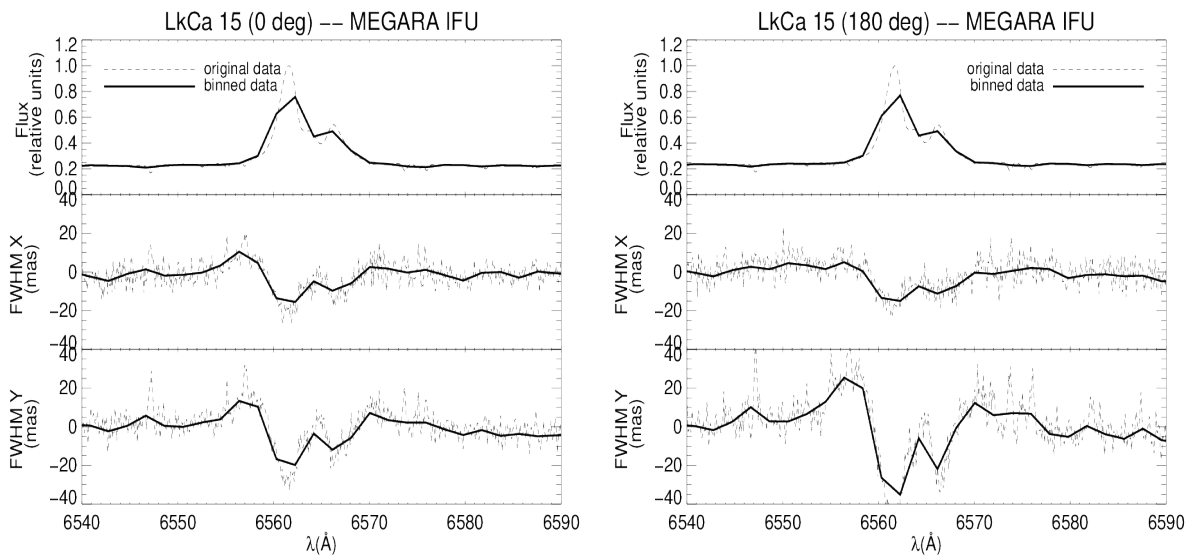

Figure 19: *Top panels show the intensity spectrum. The middle and bottom panels show the FWHM spectra centered on H_α for observations of LkCa 15 at 0° (left) and 180° (right). Original (dashed) and binned data (full line) are plotted.*

After the SA signal, let's also take a closer look at the FWHM signals, shown in Figure 19 centered on H_α for both angles. For both angles and in both the X and Y direction we observe a signal whose intensity varies between the datasets, but its shape remains the same. Note that the signal shape does not look like the one reported by Mendigutía et al. (2018).

To understand the origin of the signals observed in our photocenter and FWHM spectra, we attempt different tests. The signals might be related with short-term variability of the source, PSF distortions due to variable observing conditions or with instrumental artifacts. We explore options for both causes in the following paragraphs.

LkCa 15 is known to be a very variable source (Murphy et al. 2019), so we first investigate if the intensity changes which we observe could be caused by short term-variability. To test this, we compare the intensity spectra for the 0° and 180° dataset. The H_α line profiles and the total fluxes in a large aperture (from the central spaxel and two rings) are similar, which does not support variability.

When we compare the intensity spectrum from only the central spaxel, we see a significant decrease in flux in the 180° with respect to the 0° dataset, which could be evidence for a change in seeing conditions between the exposures. In fact, we measure a higher FWHM of the star in the 180° datacube, and the seeing monitor of the nearby WHT/INT suggests a change between the two exposures. For more details, see Appendix B. The observations started with the seeing <1.1 mas, as reported by the observatory, but it seems that the conditions changed during the observations, of course influencing our data.

To further test the variability, we plot the SA and FWHM signals from each of the six individual spectra for both angles (Figures 20 and 21). The upper panels in each Figure show the signal in the Y, and lower panels the X direction. To remove cosmic rays from the data, a median is applied for each 20 values. The plots show some remaining, as we did not have time to improve the cleaning, but this was enough for our purposes. In the 0° data we see the same SA and FWHM signal in the six spectra, and the same is true for the signals in the 180° data. Since the two datasets are different, this suggests the cause isn't variability, but rather a change in conditions.
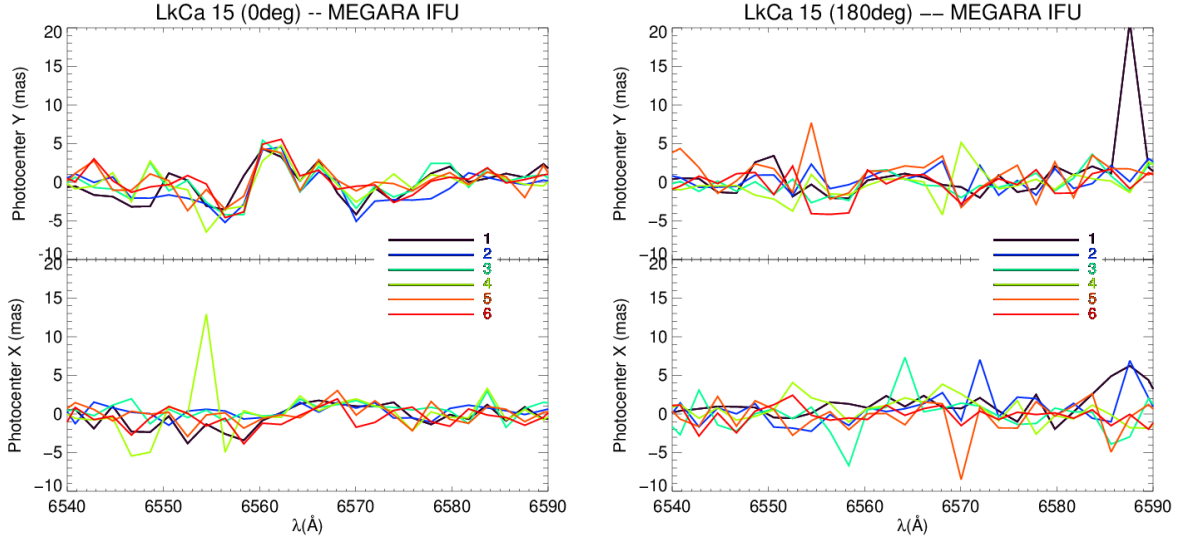
Figure 20: *Photocenter spectra centered on H_α for each of the 6 observed frames both for 0° (left) and 180° (right). The upper panels show the photocenters in the Y direction, and the lower in the X direction. The SA precision is worse in the 180° data with a higher dispersion.*
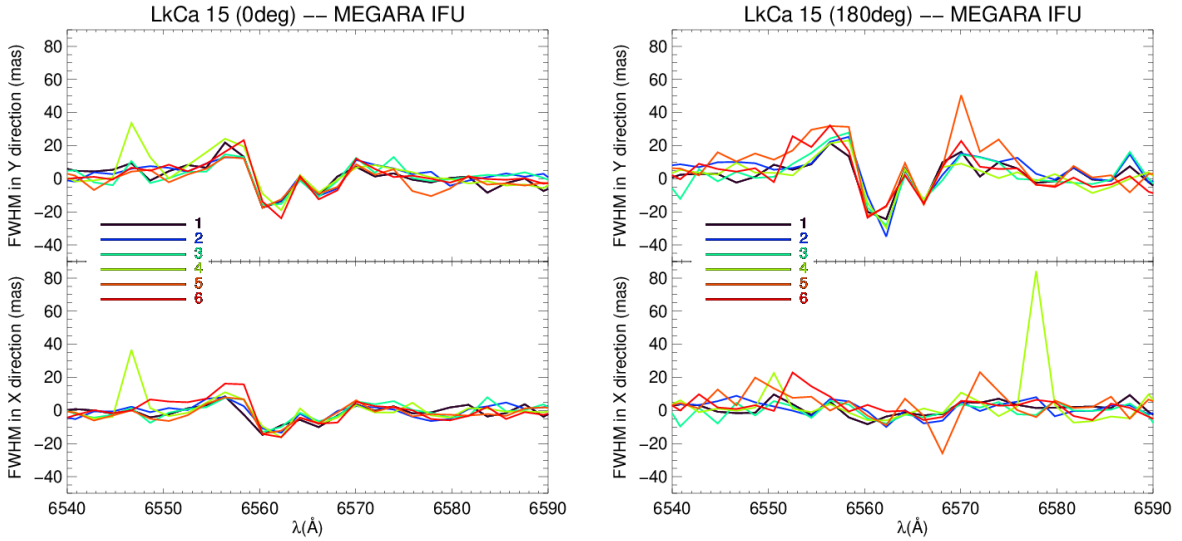

Figure 21: *FWHM spectra centered on H_α for each of the 6 observed frames both for 0° (left) and 180° (right). The upper panels show the FWHM in the Y direction, and the lower in the X direction. The SA precision is worse in the 180° data with a higher dispersion.*

We also test if some instrumental effect is causing the SA and FWHM signals in the LkCa15 data. To do so, we checked if the observed standard stars show SA signals similar to the ones observed on the scientific object. Hence, the data of HR153 and HR5501 were also fully reduced and analyzed. Since the data was reduced in the same way, a similar signal could

point towards a problem with any of the reduction steps. The intensity, photocenter and FWHM spectra of the standard stars are shown in Figure 22. The signals do not have a shape similar to the ones observed for LkCa 15, which indicates that they are not caused in any of the different calibration steps. However, we notice SA and FWHM signals in H_α for HR153, as well as additional SA signals at different spectral lines. In the case of HR5501 we also observe a FWHM signal. The origin of these signals should be further investigated to understand if they are real or indicate PSF distortions that might affect general SA studies with MEGARA.
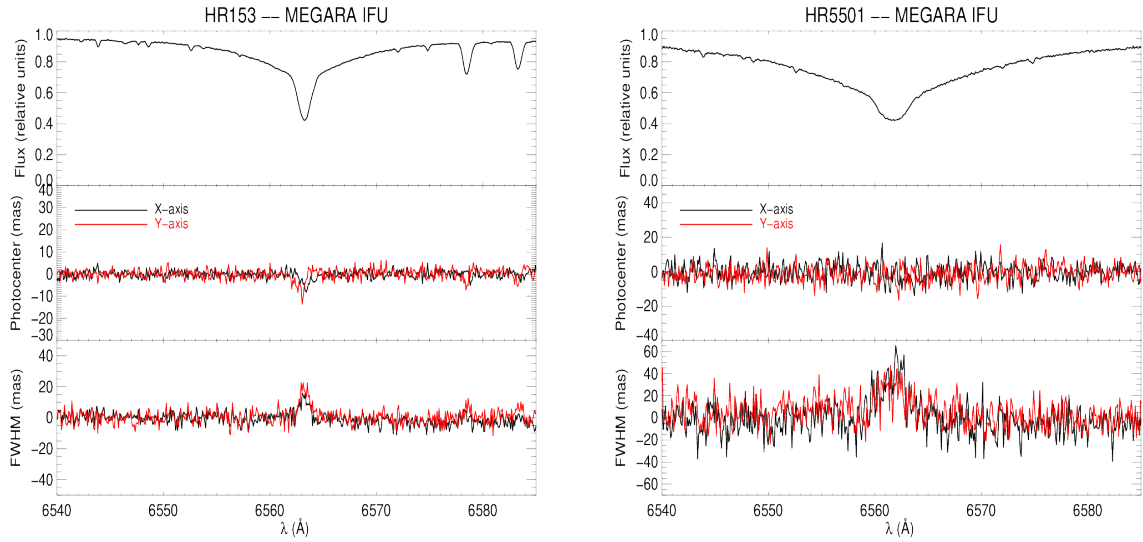

Figure 22: *Plots showing the intensity, photocenters and FWHM as functions of wavelength centered on H_α for the standard stars HR153 and HR5501. Their FWHM signals do not resemble those observed for LkCa 15.*

Another part of the process that may affect the observed signal is the conversion of the final RSS to a datacube. In that respect, we checked if changing the plate scale in this step changes the detected signal. We tested values of 0.2, 0.4, and 0.5 arcsec/pix and obtained similar results as with the chosen 0.3 arcsec/pix, meaning it does not affect the signal in the way we observe.

We contacted the MEGARA team (based at the Universidad Complutense de Madrid). We showed them our results and they will perform additional tests to further investigate if the SA and FWHM signals can have an instrumental origin. One of the tests will be to analyze the final reduced data without creating a datacube (working directly with the spaxels). Another thing they will test is if the instrumental responses of the different fibers can induce distortions in the stellar point spread function (PSF), which can be detected when performing SA. The team will check if the fibers with the poorest response can contaminate the adjacent fibers, affecting the PSF profile in this way. The proposed way to do this is to refine the *Model Map* procedure. This work is in progress and will imply writing a new routine to fit the individual fibers with more refined functions which will take into account the spectral properties of each fiber.

5 Summary and conclusions

Detecting protoplanets around young stars has proven to be a challenging task. Different observations and techniques have been used, but only two planets have so far been conclusively found, PDS 70 b,c. The first report was of three planets around the star LkCa 15 using NRM and H_α imaging by Sallum et al. (2015), but this later became a controversial result.

Spectro-astrometry is an observational technique used to very accurately measure the relative position of a source depending on wavelength. It has been used on a variety of sources, and recently showed promise for detecting protoplanets. Specifically, we look at the H_α line, which is a known tracer for accretion expected during planet formation.

As a test case, we present observations of the binary GU CMa with a well known SA signal, obtained using both the long-slit ISIS/WHT and the IFU MEGARA/GTC. Both instruments give good results, comparable to previously reported values of PA and the extent of photocenter shift. We also observed LkCa 15 using MEGARA, with the aim of testing if the instrument is well suited for detecting small protoplanet SA signals. With the help of aggressive binning, we achieve a high enough precision to be able to detect the previously reported SA signal. However, we observe a stronger signal which doesn't allow us to conclude anything about a possible accreting protoplanet. The SA signal we obtained is likely an artifact since it does not reverse in the 0 and 180 degree observations. Tests were done to investigate its origin, as well as the reason for variations in the FWHM signal, but further work is required and planned to fully understand our observations. Note that PDS 70 is a southern star not observable with the GTC, which is why we could not use it to test the MEGARA instrument.

To summarize, using the MEGARA instrument, we are able to recover strong signals from sources like a binary system. When observing smaller signals, as that expected for the LkCa 15 protoplanet candidate, we are pushing the instrument to its limits. Before we are able to conclude whether MEGARA is suitable for detecting new accreting protoplanets or not, we need to better understand the signals we observed.

5 Bibliography

Alencar, S. H. P., Bouvier, J., Donati, J. F., et al. 2018, Astronomy and Astrophysics, 620, A195

Aoyama, Y., Marleau, G.-D., Ikoma, M., & Mordasini, C. 2021, Astrophysical Journal, Letters, 917, L30

Arribas, S., Mediavilla, E., García-Lorenzo, B., del Burgo, C., & Fuensalida, J. J. 1999, Astronomy and Astrophysicss, 136, 189

Bailey, J. A. 1998, in Society of Photo-Optical Instrumentation Engineers (SPIE) Conference Series, Vol. 3355, Optical Astronomical Instrumentation, ed. S. D'Odorico, 932–939

Baines, D., Oudmaijer, R. D., Porter, J. M., & Pozzo, M. 2006, Monthly Notices of the RAS, 367, 737

Benisty, M., Bae, J., Facchini, S., et al. 2021, Astrophysical Journal, Letters, 916, L2

Benisty, M., Dominik, C., Follette, K., et al. 2022, arXiv e-prints, arXiv:2203.09991

Biller, B. A., Males, J., Rodigas, T., et al. 2014, Astrophysical Journal, Letters, 792, L22

Blakely, D., Francis, L., Johnstone, D., et al. 2022, Astrophysical Journal, 931, 3

Brannigan, E., Takami, M., Chrysostomou, A., & Bailey, J. 2006, Monthly Notices of the RAS, 367, 315

Casassus, S., Cárcamo, M., Hales, A., Weber, P., & Dent, B. 2022, Astrophysical Journal, Letters, 933, L4

Christiansen, J. L. 2022, Nature Astronomy, 6, 516

Claudi, R., Maire, A. L., Mesa, D., et al. 2019, Astronomy and Astrophysics, 622, A96

Close, L. M., Follette, K., Males, J. R., et al. 2014, in Exploring the Formation and Evolution of Planetary Systems, ed. M. Booth, B. C. Matthews, & J. R. Graham, Vol. 299, 32–33

Currie, T., Cloutier, R., Brittain, S., et al. 2015, Astrophysical Journal, Letters, 814, L27

Currie, T., Marois, C., Cieza, L., et al. 2019, Astrophysical Journal, Letters, 877, L3

Espaillat, C., Calvet, N., D'Alessio, P., et al. 2007, Astrophysical Journal, Letters, 670, L135

Garcia, P. J. V., Thiébaut, E., & Bacon, R. 1999, Astronomy and Astrophysics, 346, 892

Girard, J. H., Haffert, S. Y., Bae, J., et al. 2020, in Society of Photo-Optical Instrumentation Engineers (SPIE) Conference Series, Vol. 11448, Society of Photo-Optical Instrumentation Engineers (SPIE) Conference Series, 1144808

Gnerucci, A., Marconi, A., Capetti, A., et al. 2011, Astronomy and Astrophysics, 536, A86

Haffert, S. Y., Bohn, A. J., de Boer, J., et al. 2019, Nature Astronomy, 3, 749

Haisch, Karl E., J., Lada, E. A., & Lada, C. J. 2001, Astrophysical Journal, Letters, 553, L153

Isella, A., Chandler, C. J., Carpenter, J. M., Pérez, L. M., & Ricci, L. 2014, Astrophysical Journal, 788, 129

Keppler, M., Benisty, M., Müller, A., et al. 2018, Astronomy and Astrophysics, 617, A44

Kraus, A. L. & Ireland, M. J. 2012, Astrophysical Journal, 745, 5

Kraus, A. L., Ireland, M. J., Martinache, F., & Lloyd, J. P. 2009, in American Institute of Physics Conference Series, Vol. 1094, 15th Cambridge Workshop on Cool Stars, Stellar Systems, and the Sun, ed. E. Stempels, 453–456

Ligi, R., Vigan, A., Gratton, R., et al. 2018, Monthly Notices of the RAS, 473, 1774

Lovelace, R. V. E., Covey, K. R., & Lloyd, J. P. 2011, Astronomical Journal, 141, 51

Mendigutía, I. 2019, in Highlights on Spanish Astrophysics X, ed. B. Montesinos, A. Asensio Ramos, F. Buitrago, R. Schödel, E. Villaver, S. Pérez-Hoyos, & I. Ordóñez-Etxeberria, 359–365

Mendigutía, I., Oudmaijer, R. D., Schneider, P. C., et al. 2018, Astronomy and Astrophysics, 618, L9

Menezes, R. B., Steiner, J. E., & Ricci, T. V. 2014, Monthly Notices of the RAS, 438, 2597

Mordasini, C., Klahr, H., Alibert, Y., Benz, W., & Dittkrist, K.-M. 2010, arXiv e-prints, arXiv:1012.5281

Murphy, J., Czekala, I., Macintosh, B., Andrews, S. M., & Latham, D. W. 2019, in American Astronomical Society Meeting Abstracts, Vol. 233, American Astronomical Society Meeting Abstracts #233, 360.19

Pinte, C., Price, D. J., Ménard, F., et al. 2018, Astrophysical Journal, Letters, 860, L13

Quanz, S. P., Amara, A., Meyer, M. R., et al. 2015, Astrophysical Journal, 807, 64

Reggiani, M., Christiaens, V., Absil, O., et al. 2018, Astronomy and Astrophysics, 611, A74

Sallum, S., Follette, K. B., Eisner, J. A., et al. 2015, Nature, 527, 342

Shokry, A., Saad, S. M., Hamdy, M. A., et al. 2018, , 59, 8

Simon, M., Dutrey, A., & Guilloteau, S. 2000, Astrophysical Journal, 545, 1034

Stomski, Paul J., J., Le Mignant, D., Wizinowich, P. L., Campbell, R. D., & Goodrich, R. 2003, in Society of Photo-Optical Instrumentation Engineers (SPIE) Conference Series, Vol. 4839, Adaptive Optical System Technologies II, ed. P. L. Wizinowich & D. Bonaccini, 943–953

Szulagyi, J. & Ercolano, B. 2020, in American Astronomical Society Meeting Abstracts, Vol. 235, American Astronomical Society Meeting Abstracts #235, 121.06

Thalmann, C., Janson, M., Garufi, A., et al. 2016, Astrophysical Journal, Letters, 828, L17

Vieira, S. L. A., Corradi, W. J. B., Alencar, S. H. P., et al. 2003, Astronomical Journal, 126, 2971

Voigt, B. & Wiedemann, G. 2009, in American Institute of Physics Conference Series, Vol. 1094, 15th Cambridge Workshop on Cool Stars, Stellar Systems, and the Sun, ed. E. Stempels, 896–899

Wagner, K., Follete, K. B., Close, L. M., et al. 2018, Astrophysical Journal, Letters, 863, L8

Wheelwright, H. E., Oudmaijer, R. D., & Goodwin, S. P. 2010, Monthly Notices of the RAS, 401, 1199

Whelan, E. & Garcia, P. 2008, in Jets from Young Stars II, ed. F. Bacciotti, L. Testi, & E. Whelan, Vol. 742, 123

Whelan, E. T., Huélamo, N., Alcalá, J. M., et al. 2015, Astronomy and Astrophysics, 579, A48

Whelan, E. T., Ray, T. P., Bacciotti, F., & Jayawardhana, R. 2006, New Astronomy Review, 49, 582

Williams, J. P. & Cieza, L. A. 2011, Annual Review of Astron and Astrophys, 49, 67

Willson, M., Kraus, S., Kluska, J., et al. 2016, Astronomy and Astrophysics, 595, A9

A First MEGARA observation of LkCa 15 in 2020

LkCa 15 was observed in visitor mode in December 2020 as part of a pilot program for testing the SA capabilities of MEGARA. Unfortunatelly, the weather conditions were not good, with large changes in the seeing that varied between 1 and 3 arcsec. We obtained 24 individual spectra of 360 sec exposure time each. Due to the bad weather conditions, we did not obtain observations at a antiparallel PA of 180°.

The data was reduced in the same way as described in section 3.4, and is shown in Figure 23. The intensity spectrum showed a two peak profile of the H_α line, but with a clearly different shape than the one observed in the 2022 data. This is not surprising since LkCa 15 is known to present short- and long-term H_α variability. Alencar et al. (2018) made a series of observations ranging from November 2015. to January 2017., and show the different H_α profiles.

Spectro-astrometric result
We reported a strong SA signal in the X-axis with an amplitude of $\sim$20 mas. No SA signal was observed in the Y-direction. Note that the average SA precision in the X and Y directions was $\sim$2.0 mas. The FWHM signal was also clear in the XY-directions, with a similar shape to that seen in 2022 (see Figure 16), but with a larger amplitude.
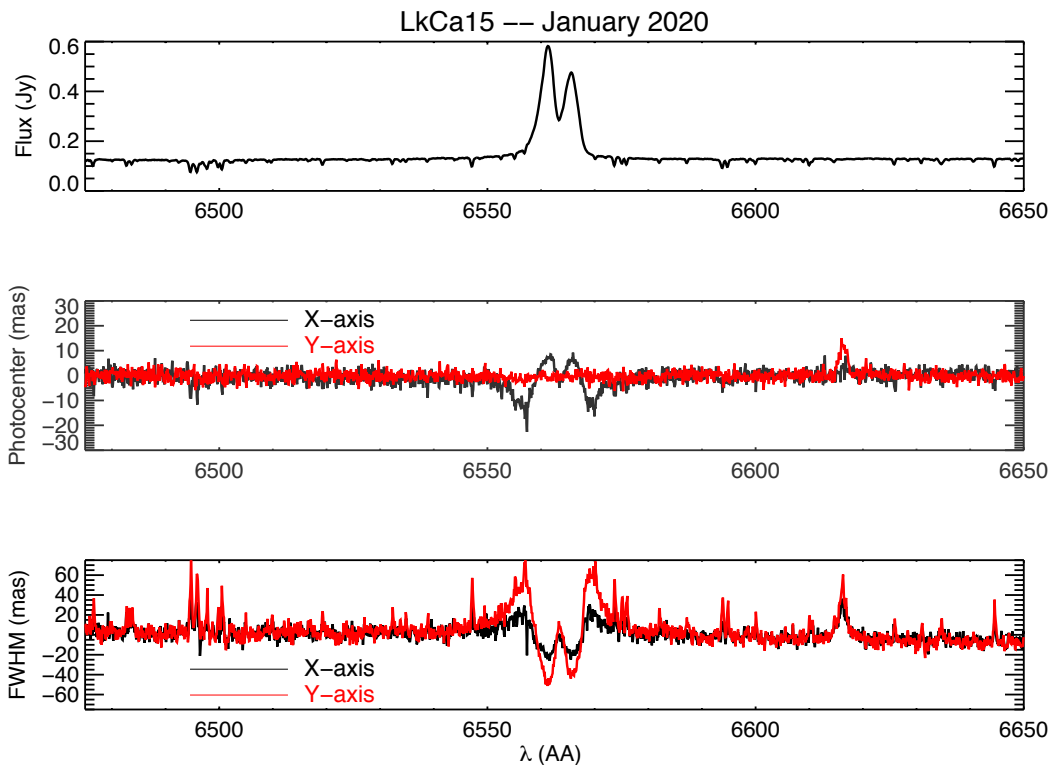

Figure 23: *The top panel shows the intensity spectrum of LkCa 15, observed in 2020. The middle and bottom panels show the photocenter and FWHM spectra in the X and Y directions.*

B Seeing conditions during the observations of LkCa 15

The seeing for the observation of LkCa 15 reported by the observatory is 1.1 mas. However, our data suggests that this value may have varied during the night, as the observation started at around 22:00 UT and lasted two hours to complete for both angles. As the GTC doesn't have data of the seeing during the night, we take a look at the seeing monitor from the nearby WHT/INT (Figure 24). The seeing indeed appears to be around 1.1 mas at the beginning of our observations, but later varies. This is in agreement with the difference for the exposures taken at 0° and 180°.
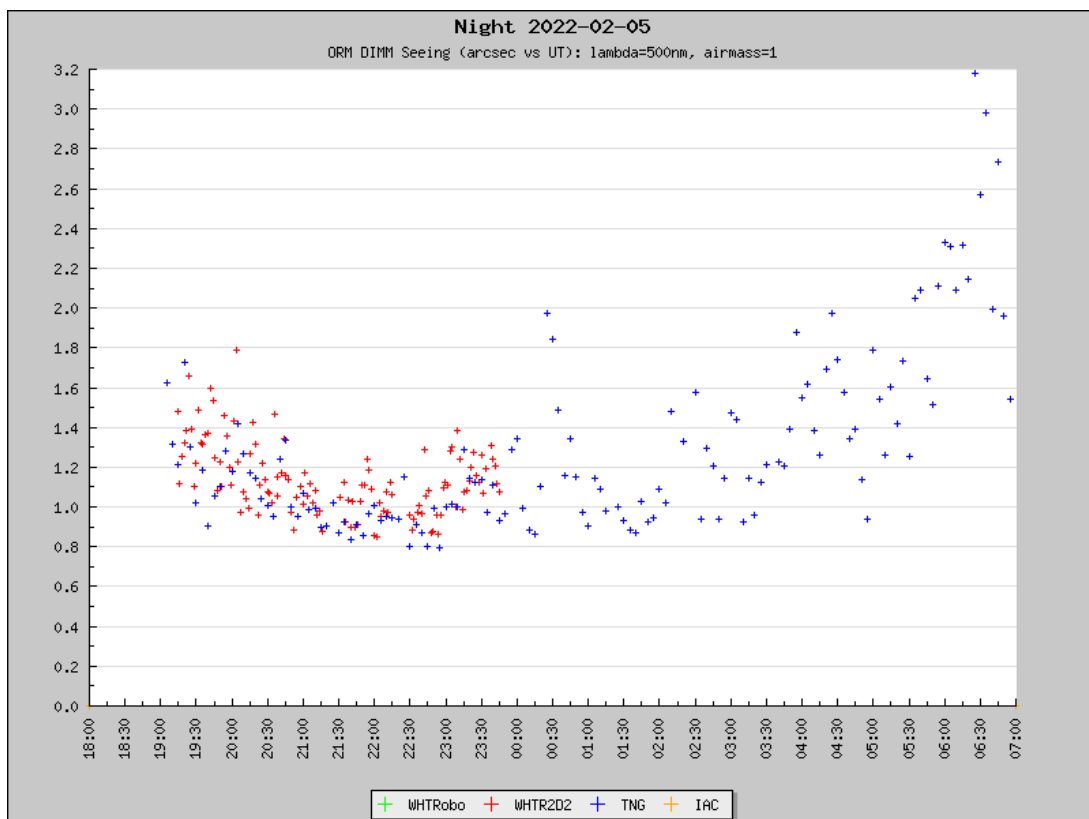

Figure 24: *Seeing conditions on the 5th of February 2022 at WHT/INT. Observations of LkCa 15 were done between 22:00 UT and midnight.*